

Mapping quantum state dynamics in spontaneous emission

M. Naghiloo,¹ N. Foroozani,¹ D. Tan,¹ A. Jadbabaie,¹ and K. W. Murch^{*1,2}

¹*Department of Physics, Washington University, St. Louis, Missouri 63130*

²*Institute for Materials Science and Engineering, St. Louis, Missouri 63130*

(Dated: December 8, 2024)

The evolution of a quantum state undergoing radiative decay depends on how the emission is detected. We employ phase-sensitive amplification to perform homodyne detection of the spontaneous emission from a superconducting artificial atom. Using quantum state tomography, we characterize the correlation between the detected homodyne signal and the emitter's state, and map out the conditional back-action of homodyne measurement. By tracking the diffusive quantum trajectories of the state as it decays, we characterize selective stochastic excitation induced by the choice of measurement basis. Our results demonstrate dramatic differences from the quantum jump evolution that is associated with photodetection and highlight how continuous field detection can be harnessed to control quantum evolution.

In spontaneous emission, an emitter decays from an excited state by releasing radiation into a quantized mode of the electromagnetic field. From the point of view of quantum measurement theory, the light-matter interaction entangles the quantum state of the emitter with its electromagnetic environment^{1,2}. Subsequent measurements of the field convey information about the state of the emitter and consequently cause back-action³. Typically, spontaneous emission is detected in the form of energy quanta, resulting in an instantaneous jump of the emitter to a lower energy state. However, if the emission is measured with a detector that is not sensitive to quanta, but rather to the amplitude of the field, the emitter's state undergoes different dynamics over finite timescales. Here, we use a near-quantum-limited Josephson parametric amplifier to perform continuous homodyne measurements of the spontaneous emission from a superconducting artificial atom. Under such detection, the emitter does not undergo jumps to its ground state, but rather diffuses through its state space. Furthermore, phase-sensitive operation of the amplifier squeezes the monitored field, inducing selective back-action on the emitter's state^{4,5}. We use quantum state tomography and weak measurements to map out the conditional evolution and to track individual quantum trajectories^{3,6,7} of the emitter's state, giving insight into spontaneous emission and routes to control this light-matter interaction.

The entanglement between a quantum emitter and its spontaneous emission field has been studied in experiments using natural atoms¹ and in solid state systems², and can be used to herald entanglement between spatially separated systems⁸. Spontaneous emission depends intimately on the fluctuations of the electromagnetic vacuum, and several experiments have controlled this process by either altering vacuum fluctuations⁹ or engineering the electromagnetic environment^{10–13}. Emission can also be viewed in the context of quantum measurement; the light-matter interaction entangles the quantum state of the emitter with the quantized modes of the electromagnetic field³. The entangled electromagnetic modes serve as a quantum pointer system; subsequent measurements of the field convey information about the emit-

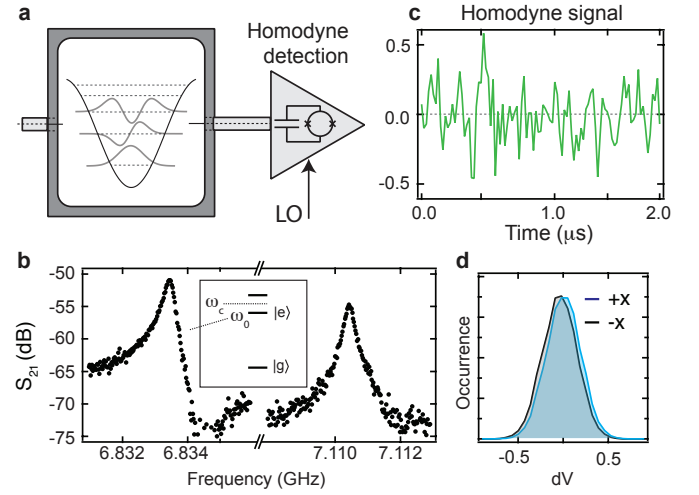


Figure 1: Experimental setup. **a**, The experiment uses the effective two-level system formed by the resonant interaction between the lowest energy transition of a transmon circuit and the TE_{101} mode of a microwave cavity. **b**, The transmission spectrum of the system, reveals the two polariton states and we focus on the lowest energy transition as our quantum emitter. **c**, The radiative decay of the system is monitored with a near-quantum limited parametric amplifier in phase-sensitive operation that performs homodyne measurement. **d**, Histogram of the detected homodyne signal dV that is obtained when the emitter is prepared in either the $+x$ or $-x$ eigenstates.

ter and cause back-action^{7,14,15}. Therefore, the choice of measurement on the field can affect the evolution of the emitter's state⁵.

In this work, we perform homodyne measurements of spontaneous emission from an effective two-level system, formed by the strong light-matter interaction between a superconducting circuit and a microwave cavity. By performing phase-sensitive amplification, we selectively amplify and de-amplify orthogonal quadratures of the emission field, thus limiting the measurement back-action experienced by the emitter^{7,16}. We use quantum

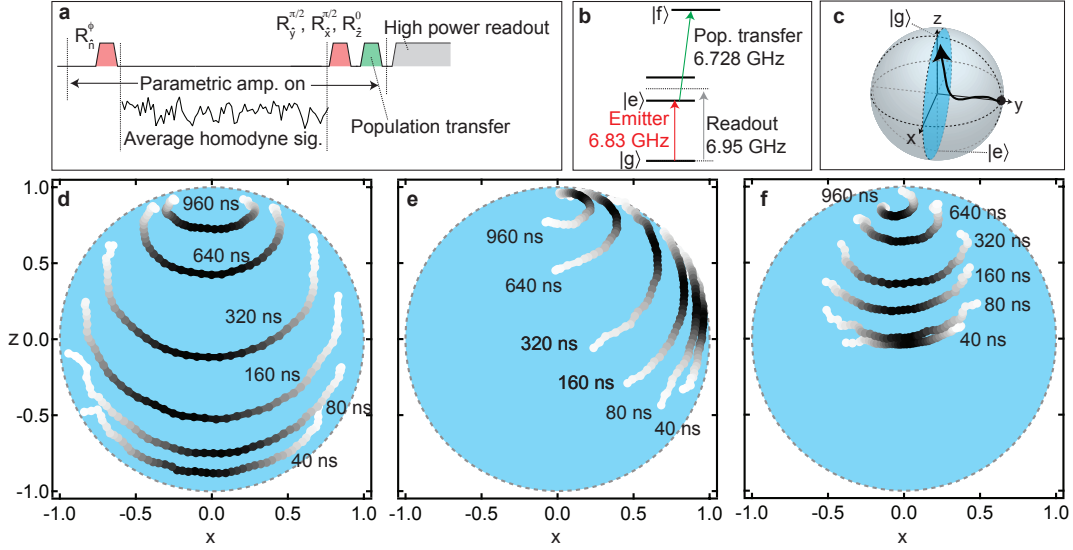


Figure 2: **Mapping spontaneous decay.** **a**, The experiment sequence prepares the emitter in an initial state and homodyne detection is used to record the emitted radiation. Following a variable period of time, further rotations are applied to the emitter before state readout to perform quantum state tomography on the state. To enhance the readout contrast a π pulse is applied to move the excited state population to a higher state of the system. **b**, The level structure of the system and frequencies of the three microwave drives. **c**, We average the state tomography we determine $x \equiv \langle \sigma_x \rangle|_{\bar{V}}$, and $z \equiv \langle \sigma_z \rangle|_{\bar{V}}$ conditioned on the outcome of the homodyne measurement. These correlated tomography results are displayed on the x - z plane of the Bloch sphere for three different initial states: $-z$ (**d**), $+x$ (**e**), and $+y$ (**f**). The color scale indicates the relative occurrence of the of the each measurement value. Note the different backaction between (**e**), and $+y$ (**f**), a result of phase-sensitive amplification.

state tomography, in addition to weak measurements, to study the back-action of homodyne measurements and track the time evolution of the emitter's state under radiative decay. Contrary to the quantum jump evolution associated with photodetection, we observe quantum trajectories^{3,7,17} that stochastically diffuse through the state space of the emitter. For certain phases of homodyne detection we observe that the emitter evolves toward its excited state under radiative decay⁴.

Our system consists of a transmon circuit¹⁸ resonantly coupled to a three dimensional waveguide cavity¹⁹. The strong light-matter interaction between the circuit and the cavity strips them of their individual character and gives rise to hybrid circuit-cavity states, as shown in Fig. 1. We use the lowest energy transition ($\omega_0/2\pi = 6.83$ GHz) as an effective two-level system; deliberate coupling to a 50Ω transmission line results in a radiative decay rate $\gamma = 2.3 \times 10^6 \text{ s}^{-1}$. This electromagnetic emission is described by the interaction Hamiltonian, $H_{\text{int}} = \gamma(a^\dagger \sigma_- + a \sigma_+)$, where a^\dagger (a) is the creation (annihilation) operator for a photon in the transmission line, and σ_+ (σ_-) are the pseudo-spin raising (lowering) operators for the effective two-level system. The radiation from the emitter is then amplified by a near-quantum-limited Josephson parametric amplifier^{20,21}. We perform phase-sensitive amplification²² for signals near the emission frequency, amplifying and measuring the field quadrature $a^\dagger e^{i\phi} + a e^{-i\phi}$, which, by virtue of the emitter-field interaction, is sensitive to a specific quadrature of the emitter's dipole, $\sigma_+ e^{i\phi} + \sigma_- e^{-i\phi}$.

To demonstrate that our homodyne detection scheme is sensitive to a single quadrature of the emitter's dipole, we prepare the emitter in a specific state, amplify the radiative emission with a local oscillator phase $\phi = 0$, and integrate the resulting signal. By repeating the measurement for several iterations, we create histograms of the homodyne signal. We compare the resulting distributions for two state preparations, $\pm x$ (the positive or negative eigenstates of σ_x Pauli operator), as shown in Fig 1. The width of the resulting Gaussian histograms originates from both the quantum fluctuations of the detected mode and noise added in the amplification chain. We scale the dimensionless signal such that its variance is $\sigma^2 = \gamma dt$, where $dt = 20 \text{ ns}$ is the integration time. The resulting separation of the two histograms, $\Delta V = 2\sqrt{\eta}\gamma dt$, gives the quantum efficiency of our detection setup as $\eta = 30\%$.

To map the conditional dynamics of the emitter's state under radiative decay, we conduct the experimental sequence depicted in Fig. 2a. We first use a resonant rotation to prepare an initial state, then proceed to obtain the average homodyne signal \bar{V} by integrating the detected homodyne signal for a variable period of time, and finally perform projective measurements to conduct quantum state tomography as described in the methods. The results of these projective measurements are averaged conditionally on the integrated homodyne signal. This yields the conditional Pauli averages, $\langle \sigma_x \rangle|_{\bar{V}}$, $\langle \sigma_y \rangle|_{\bar{V}}$, $\langle \sigma_z \rangle|_{\bar{V}}$. In Fig. 2d-e we plot $\langle \sigma_z \rangle|_{\bar{V}}$ and $\langle \sigma_x \rangle|_{\bar{V}}$ parametrically on the x - z plane of the Bloch sphere for different integration times. We study the conditional evolution for three

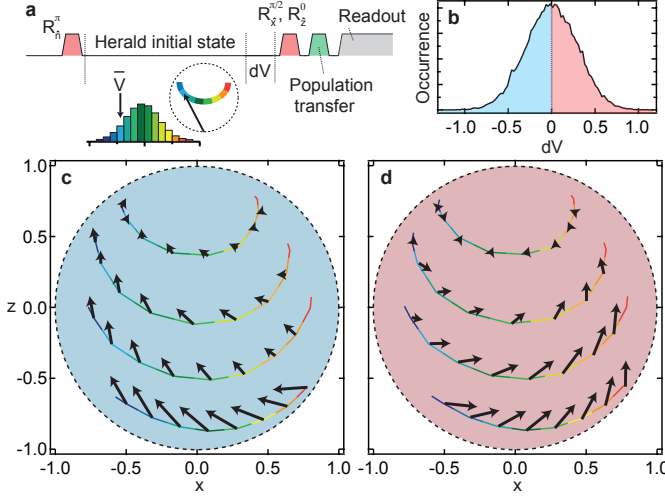


Figure 3: **Back-action vector maps.** **a**, An arbitrary initial state in the Bloch sphere is prepared by heralding on the average homodyne signal \bar{V} . Quantum state tomography is used to examine the conditional back-action based on a small portion of the signal dV . **b**, Histogram of the signals dV which we separate into positive or negative dV . The back-action imparted on the emitter for negative (c) or positive (d) values of dV is depicted by an arrow at different locations in the x - z plane of the Bloch sphere.

different state preparations.

When the emitter is prepared in the excited state (along the $-z$ axis of the Bloch sphere, (Fig. 2d)), the x -component of the state develops a correlation with the average homodyne signal. This highlights how our homodyne measurement provides an indirect signature²³ of only the real part of $\sigma_- = (\sigma_x + i\sigma_y)/2$. As the state is allowed more time to decay, it evolves to different deterministic arcs in the interior of the Bloch sphere. When the emitter is prepared in the state $+x$ (Fig. 2e), we observe that some of the conditioned states evolve toward the excited state⁴. This stochastic excitation is unique to amplitude measurements of the field quadrature, since such excitation is not possible under photodetection²³.

Under phase-sensitive amplification, the choice of homodyne phase can vary the stochastic back-action on the emitter's state. To study this, we prepare the emitter in the state y , an eigenstate of the imaginary part of our measured operator $\sigma_- = (\sigma_x + i\sigma_y)/2$. This emitter dipole quadrature corresponds to the de-amplified quadrature of the emission field, and therefore no stochastic excitation is observed (Fig. 2f).

We take advantage of the deterministic evolution of the emitter, conditioned on the integrated homodyne signal, to characterize the back-action at different points in the Bloch sphere. Figure 3 shows a vector map of the state evolution due to a specific detected homodyne signal dV at various points. By preparing the emitter in the excited state and averaging the homodyne detection for various periods of time, we can prepare a nearly arbitrary mixed state through heralding. After selecting a decay time and

a specific initial state (x_i, z_i) , based on an average signal \bar{V} , we digitize the homodyne signal for an additional time $dt = 40$ ns to obtain dV . We then use quantum state tomography to determine the final state (x_f, z_f) , conditioned on the detection of dV within a specified range. The back-action at a specific location in state space, associated with the detection of a given value of dV , is provided by the vector connecting (x_i, z_i) and (x_f, z_f) . The back-action vector maps demonstrate how positive measurement results push the state toward the $+x$ axis. Furthermore, the maps show the back-action is stronger near the $-z$ axis of the Bloch sphere, indicating that the measurement strength is proportional the emitter's excitation.

The back-action maps that we present in Fig. 3 allow us to calculate the evolution of the emitter's state conditioned on a sequence of homodyne measurement results. Formally, this evolution is described by a stochastic master equation⁴,

$$d\rho = \gamma \mathcal{D}[\sigma_-]\rho dt + \sqrt{\eta}\gamma \mathcal{H}[\sigma_- dW_t]\rho. \quad (1)$$

Where $\mathcal{D}[\sigma_-]\rho = \sigma_- \rho \sigma_+ - \frac{1}{2}(\sigma_+ \sigma_- \rho + \rho \sigma_+ \sigma_-)$ and $\mathcal{H}[O]\rho = O\rho + \rho O^\dagger - \text{tr}[(O + O^\dagger)\rho]\rho$ are the dissipation and jump superoperators, respectively. When we ignore the results of homodyne monitoring (for example by setting $\eta = 0$), the state follows deterministic evolution from an initial state to the ground state, as described by the first term of Eq. (1). The second term accounts for information conveyed by the homodyne measurement through stochastic noise increments dW_t , which are independent, zero-mean, Gaussian distributed Wiener increments with variance dt . Our homodyne signal dV_t , detected in a time step dt , is proportional to the real part of σ_- for the emitter, $dV_t = \sqrt{\eta}\gamma \langle \sigma_x \rangle dt + \sqrt{\gamma} dW_t$. We can recast this stochastic master equation in terms of the Bloch vector components x, z, y ,

$$dx = -\frac{\gamma}{2}xdt + \sqrt{\eta}(1-z-x^2)(dV_t - \gamma\sqrt{\eta}xdt), \quad (2)$$

$$dz = \gamma(1-z)dt + \sqrt{\eta}x(1-z)(dV_t - \gamma\sqrt{\eta}xdt), \quad (3)$$

$$dy = -\frac{\gamma}{2}ydt - \sqrt{\eta}xy(dV_t - \gamma\sqrt{\eta}xdt). \quad (4)$$

We now turn to calculating individual quantum trajectories for the emitter's state as it evolves from an initial state to the final ground state. In Fig. 4, we prepare the emitter in the excited state and then digitize the detected homodyne signal for $2 \mu\text{s}$. Based on this signal, we use Eqs. (2,3,4) to calculate the emitter's trajectory using time steps of $dt = 20$ ns. Instead of taking a straight path to the ground state, the trajectory diffuses through the Bloch sphere, subject to back-action from the measured quantum fluctuations of the emission field. As described in the methods, we use conditional quantum state tomography to verify that these individual trajectories make the correct predictions for all possible measurements at each time. As shown in Fig. 4, the tomographic validation is in good agreement with the individual trajectories, reproducing their specific stochastic behavior.

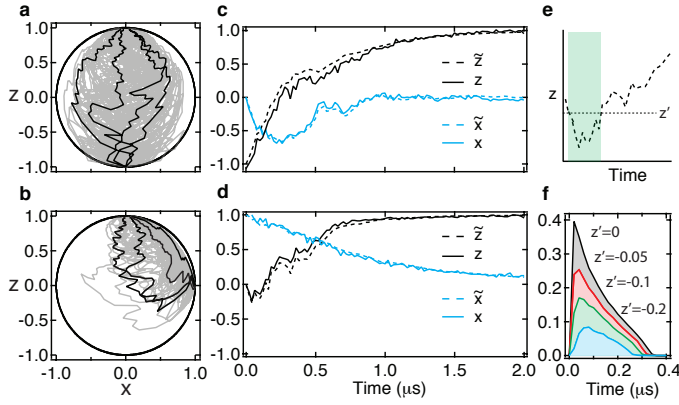


Figure 4: **Quantum trajectories.** **a,b**, Quantum trajectories of spontaneous decay calculated by the stochastic master equation, initiated from $-z$ (**a**) and $+x$ (**b**). Several trajectories are depicted in gray, and a few individual trajectories are highlighted in black. **c,d** Individual trajectories (dashed) that originate from $-z$ (**c**) and $+x$ (**d**) and the tomographic reconstruction (solid) based on projective measurements. **e**, For trajectories that are initiated along $+x$ some are excited (attaining values below a threshold z'). **f**, Fraction of the trajectories that are excited below the threshold z' versus time.

We also study quantum trajectories originating from the state $+x$. In this case, the stochastic back-action causes some of the trajectories to become more excited as they decay under homodyne detection. In Fig. 4f, we quantify this feature by extracting the probability of excitation above a certain threshold at different times. To better understand this behavior, we examine the measurement term in Eq. 3, proportional to $\sqrt{\eta}$. In terms of Weiner increments, the state at $+x$ will be stochas-

tically excited if the measurement noise dW_t , obtained from the detected signal dV_t , is less than $-\sqrt{\gamma/\eta}dt$, predicting that $\sim 35\%$ of the trajectories should be excited in the first time step.

Recent experiments^{6,7,17,24–26} that harness Bayesian statistics or use quantum optics to track the evolution of quantum states have yielded a deeper understanding of quantum measurement evolution. Here, we have shown how specific quadrature measurements of the fluorescence from a quantum emitter result in a rich conditional evolution of the state—and we have harnessed this evolution to map out the back-action associated with such measurements, tracking the individual quantum trajectories an emitter takes when decaying through fluorescence. In contrast to the instantaneous dynamics of emission due to measurements of quanta, here we show that spontaneous emission may also occur over finite timescales.

Measurements, and more broadly, control over a quantum environment, can in principle be used to steer quantum evolution^{27,28}. Phase-sensitive parametric amplification squeezes the quantum pointer state and therefore causes selective measurement back-action on the emitter. Such control over the quantum light-matter interaction has the potential to advance techniques in fluorescence based imaging, and will be essential in quantum feedback control^{3,16,29} of quantum systems.

Acknowledgements We thank A. N. Jordan and K. Mølmer for discussions. This research was supported in part by the John F. Templeton Foundation and the Sloan Foundation and used facilities at the Institute of Materials Science and Engineering at Washington University.

Correspondence and requests for materials should be addressed to K.W.M. (murch@physics.wustl.edu)

- ¹ B. B. Blinov, D. L. Moehring, L.-M. Duan, and C. Monroe. Observation of entanglement between a single trapped atom and a single photon. *Nature*, 428:153–157, 2004.
- ² C. Eichler, C. Lang, J. M. Fink, J. Govenius, S. Filipp, and A. Wallraff. Observation of entanglement between itinerant microwave photons and a superconducting qubit. *Phys. Rev. Lett.*, 109:240501, Dec 2012.
- ³ H. Wiseman and G. Milburn. *Quantum Measurement and Control*. Cambridge University Press, 2010.
- ⁴ Anders Bolund and Klaus Mølmer. Stochastic excitation during the decay of a two-level emitter subject to homodyne and heterodyne detection. *Phys. Rev. A*, 89:023827, Feb 2014.
- ⁵ Howard M. Wiseman and Jay M. Gambetta. Are dynamical quantum jumps detector dependent? *Phys. Rev. Lett.*, 108:220402, May 2012.
- ⁶ C. Guerlin, J. Bernu, S. Deleglise, C. Sayrin, S. Gleyzes, S. Kuhr, M. Brune, J. Raimond, and S. Haroche. Progressive field-state collapse and quantum non-demolition photon counting. *Nature*, 448:889, 2007.
- ⁷ K. W. Murch, S. J. Weber, C. Macklin, and I. Siddiqi. Observing single quantum trajectories of a superconducting

- qubit. *Nature*, 502:211, 2013.
- ⁸ H. Bernien, B. Hensen, W. Pfaff, G. Koolstra, M. S. Blok, L. Robledo, T. H. Taminiau, M. Markham, D. J. Twitchen, L. Childress, and R. Hanson. Heralded entanglement between solid-state qubits separated by three metres. *Nature*, 497:86–90, 2013.
- ⁹ K. W. Murch, S. J. Weber, K. M. Beck, E. Ginossar, and I. Siddiqi. Reduction of the radiative decay of atomic coherence in squeezed vacuum. *Nature*, 499:62–65, 2013.
- ¹⁰ E. M. Purcell. Spontaneous emission probabilities at radio frequencies. *Phys. Rev.*, 69:681, 1946.
- ¹¹ A. A. Houck, D. I. Schuster, J. M. Gambetta, J. A. Schreier, B. R. Johnson, J. M. Chow, L. Frunzio, J. Majer, M. H. Devoret, S. M. Girvin, and R. J. Schoelkopf. Generating single microwave photons in a circuit. *Nature*, 449:328–331, 2007.
- ¹² A. A. Houck, J. A. Schreier, B. R. Johnson, J. M. Chow, Jens Koch, J. M. Gambetta, D. I. Schuster, L. Frunzio, M. H. Devoret, S. M. Girvin, and R. J. Schoelkopf. Controlling the spontaneous emission of a superconducting transmon qubit. *Phys. Rev. Lett.*, 101:080502, Aug 2008.
- ¹³ I.-C. Hoi, A. F. Kockum, L. Tornberg, A. Pourkabirian,

- G. Johansson, P. Delsing, and C. M. Wilson. Probing the quantum vacuum with an artificial atom in front of a mirror. *Nature Physics*, page 3484, 2015.
- 14 M. Hatridge, S. Shankar, M. Mirrahimi, F. Schackert, K. Geerlings, T. Brecht, K. M. Sliwa, B. Abdo, L. Frunzio, S. M. Girvin, R. J. Schoelkopf, and M. H. Devoret. Quantum back-action of an individual variable-strength measurement. *Science*, 339(6116):178–181, 2013.
 - 15 J. P. Groen, D. Ristè, L. Tornberg, J. Cramer, P. C. de Groot, T. Picot, G. Johansson, and L. DiCarlo. Partial-measurement backaction and nonclassical weak values in a superconducting circuit. *Phys. Rev. Lett.*, 111:090506, Aug 2013.
 - 16 G. de Lange, D. Ristè, M. J. Tiggelman, C. Eichler, L. Tornberg, G. Johansson, A. Wallraff, R. N. Schouten, and L. DiCarlo. Reversing quantum trajectories with analog feedback. *Phys. Rev. Lett.*, 112:080501, Feb 2014.
 - 17 S. J. Weber, A. Chantasri, J. Dressel, A. N. Jordan, K. W. Murch, and I. Siddiqi. Mapping the optimal route between two quantum states. *Nature*, 511:570D573, 2014.
 - 18 Jens Koch, Terri M. Yu, Jay Gambetta, A. A. Houck, D. I. Schuster, J. Majer, Alexandre Blais, M. H. Devoret, S. M. Girvin, and R. J. Schoelkopf. Charge-insensitive qubit design derived from the cooper pair box. *Phys. Rev. A*, 76:042319, Oct 2007.
 - 19 Hanhee Paik, D. I. Schuster, Lev S. Bishop, G. Kirchmair, G. Catelani, A. P. Sears, B. R. Johnson, M. J. Reagor, L. Frunzio, L. I. Glazman, S. M. Girvin, M. H. Devoret, and R. J. Schoelkopf. Observation of high coherence in josephson junction qubits measured in a three-dimensional circuit qed architecture. *Phys. Rev. Lett.*, 107:240501, Dec 2011.
 - 20 M. A. Castellanos-Beltran, K. D. Irwin, G. C. Hilton, L. R. Vale, and K. W. Lehnert. Amplification and squeezing of quantum noise with a tunable josephson metamaterial. *Nature Physics*, 4:929–931, 2008.
 - 21 M. Hatridge, R. Vijay, D. H. Slichter, John Clarke, and I. Siddiqi. Dispersive magnetometry with a quantum limited squid parametric amplifier. *Phys. Rev. B*, 83:134501, Apr 2011.
 - 22 A. A. Clerk, M. H. Devoret, S. M. Girvin, Florian Marquardt, and R. J. Schoelkopf. Introduction to quantum noise, measurement, and amplification. *Rev. Mod. Phys.*, 82:1155–1208, Apr 2010.
 - 23 Andrew N. Jordan, Areeya Chantasri, Pierre Rouchon, and Benjamin Huard. Anatomy of fluorescence: Quantum trajectory statistics from continuously measuring spontaneous emission. *arXiv:1511.06677*, 2015.
 - 24 N. Katz, M. Ansmann, Radoslaw C. Bialczak, Erik Lucero, R. McDermott, Matthew Neeley, Matthias Steffen, E. M. Weig, A. N. Cleland, John M. Martinis, and A. N. Korotkov. Coherent state evolution in a superconducting qubit from partial-collapse measurement. *Science*, 312(5779):1498–1500, 2006.
 - 25 N. Roch, E. Schwartz, M. F. Motzoi, C. Macklin, R. Vijay, W. Eddins, A. N. Korotkov, A. B. Whaley, K. M. Sarovar, and I. Siddiqi. Observation of measurement-induced entanglement and quantum trajectories of remote superconducting qubits. *Phys. Rev. Lett.*, 112:170501, Apr 2014.
 - 26 P. Campagne-Ibarcq, P. Six, L. Bretheau, A. Sarlette, M. Mirrahimi, P. Rouchon, and B. Huard. Observing quantum state diffusion by heterodyne detection of fluorescence. *arXiv:1511.01415*, 2015.
 - 27 W.S. Warren, H. Rabitz, and M. Dahleh. Coherent control of quantum dynamics: The dream is alive. *Science*, 259:1581–1589, 1993.
 - 28 Moshe Shapiro and Paul Brumer. *Quantum Control of Molecular Processes*. Wiley-VCH Verlag GmbH & Co. KGaA, 2011.
 - 29 R. Vijay, C. Macklin, D. H. Slichter, S. J. Weber, K. W. Murch, R. Naik, A. N. Korotkov, and I. Siddiqi. Stabilizing rabi oscillations in a superconducting qubit using quantum feedback. *Nature*, 490:77, 2012.
 - 30 K. Geerlings, Z. Leghtas, I. M. Pop, S. Shankar, L. Frunzio, R. J. Schoelkopf, M. Mirrahimi, and M. H. Devoret. Demonstrating a driven reset protocol for a superconducting qubit. *Phys. Rev. Lett.*, 110:120501, Mar 2013.
 - 31 M. D. Reed, L. DiCarlo, B. R. Johnson, L. Sun, D. I. Schuster, L. Frunzio, and R. J. Schoelkopf. High-fidelity readout in circuit quantum electrodynamics using the jaynes-cummings nonlinearity. *Phys. Rev. Lett.*, 105:173601, Oct 2010.

Supplemental Information

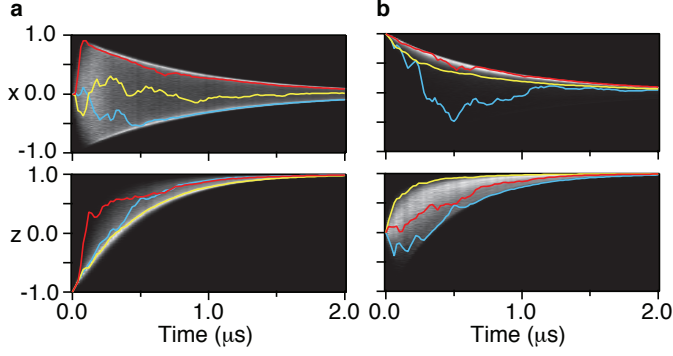
Device fabrication and parameters

The emitter system consists of a transmon circuit characterized by charging energy $E_C/h = 270$ MHz and Josephson energy $E_J/h = 24.6$ GHz. The circuit was fabricated by double angle evaporation of aluminum on a high resistivity silicon substrate. The circuit was then placed at the center of a waveguide cavity (dimensions $34.15 \times 27.9 \times 5.25$ mm) machined from 6061 aluminum. The cavity geometry was chosen to be resonant with the lowest energy transition of the transmon circuit. The resonant interaction between the circuit and the cavity (characterized by coupling rate $g/2\pi = 136$ MHz) results in hybrid states, as described by the Jaynes-Cummings Hamiltonian. The cavity is deliberately coupled to 50 Ω cables: one weakly coupled port, characterized by coupled quality factor $Q_c \simeq 10^5$, is used to drive the system, while a more strongly coupled port $Q_c \simeq 10^4$ sets the total radiative decay time of the system. This configuration results in an effectively "one dimensional atom", where all of the radiative decay is captured by the strongly coupled cable⁹. Spontaneous emission from this "artificial atom" is amplified by a near-quantum-limited Josephson parametric amplifier, consisting of a 1.5 pF capacitor, shunted by a Superconducting Quantum Interference Device (SQUID) composed of two $I_0 = 1$ μ A Josephson junctions. The amplifier is operated with negligible flux threading the SQUID loop and produces 20 dB of gain with an instantaneous 3-dB-bandwidth of 20 MHz.

We used standard techniques to measure the energy decay time $T_1 = 430$ ns and Ramsey decay time $T_2^* = 830$ ns, indicating that the sample experiences a negligibly small amount of pure dephasing. We also examined the equilibrium state populations of the emitter using a Rabi driving technique³⁰, and found the excited state population to be $< 3\%$.

State tracking

We use a master equation (equivalent to Eqs. (2-4)) to propagate the density matrix for the emitter's state



Extended Data Figure 1: **State histograms.** Greyscale histograms represent the distribution for values of x and z at each time point. The greyscale shading is normalized such that the most frequent value is 1 at each time point. **a**, Histograms of the state when the emitter is initialized in the state $-z$ with a few sample trajectories shown in color. **b**, Histograms associated with decay from the excited state $+x$.

conditioned on the detected homodyne signal. The signal is digitized in 20 ns steps, and scaled such that its variance is γdt . At each time step, we update the density matrix components $\rho_{11}[i]$ and $\rho_{01}[i]$ based on the detected measurement signal $dV[i]$, where $z \equiv 1 - \rho_{11}$ and $x \equiv 2\text{Re}[\rho_{01}]$

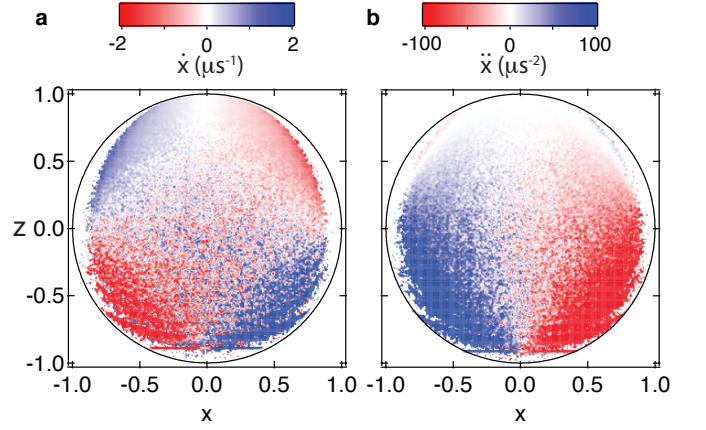
$$\begin{aligned} \rho_{11}[i+1] = & \rho_{11}[i] - \gamma \rho_{11}[i] dt \\ & - \sqrt{\eta}(dV[i] - \sqrt{\eta}\gamma 2\rho_{01}[i]dt) \\ & \times (2\rho_{01}[i]\rho_{11}[i]) \end{aligned} \quad (5)$$

$$\begin{aligned} \rho_{01}[i+1] = & \rho_{01}[i] - \gamma \rho_{01}[i]/2dt \\ & + \sqrt{\eta}(dV[i] - \sqrt{\eta}\gamma 2\rho_{01}[i]dt) \\ & \times (\rho_{11}[i] - 2\rho_{01}[i]\rho_{01}[i]) \end{aligned} \quad (6)$$

Ensemble dynamics

Based on 8.6×10^3 repetitions of the experiment and associated quantum trajectories, we can examine ensemble dynamics of the paths on the Bloch sphere taken by our decaying emitter. The behavior of single trajectories characterizes the dynamics of spontaneous decay subject to homodyne detection, and is distinctly different than the full ensemble behavior that decays deterministically toward the ground state.

Extended Data Figure 1 displays greyscale histograms of the state at different points in time for two different initial conditions. For trajectories initialized in $-z$ (Extended Data Fig. 1a), these histograms demonstrate how the decay paths are restricted to a deterministic arc in the Bloch sphere. Curiously enough, a state prepared in a traditional eigenstate of spontaneous emission will develop some quantum coherence when monitored under homodyne detection. The x -components of such trajectories may be pinned to the edges of this arc on the x axis, or instead may oscillate between the two edges. Regardless, this stochastic coherence is limited by a decreasing upper bound. Similarly, along the z axis, though some trajectories may decay in less time by more quickly ap-



Extended Data Figure 2: **Spontaneous decay dynamics.** Color maps of the ensemble average of the x -component of the velocity (**a**) and acceleration (**b**) versus location of the emitter's state.

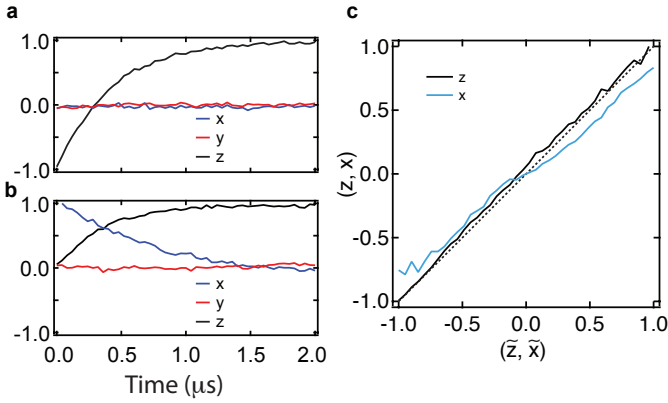
proaching a given coordinate, no trajectory may decay more slowly in z than a specific lower bound at each time step.

On the other hand, when the emitter is initialized along $+x$ in a superposition of its excited and ground states, the histograms of the Bloch sphere coordinates show different behavior (Extended Data Fig. 1b). The x -component of the trajectory encounters a decreasing upper bound on its maximum value, once more illustrating motion along a shrinking deterministic arc. The z -component, however, can exhibit extremely varied behavior. In addition to following the average decay path, the state may also stochastically excite, or it may rapidly decay in z while approaching the surface of the Bloch sphere. Currently, it is these states that rapidly decay which have the highest purity on average, retaining the most information about the state. In comparison, due to our limited measurement efficiency, stochastically excited trajectories become more mixed as they diffuse toward the excited state. We note that for $\eta = 1$, all of our trajectories, regardless of dynamics, would describe pure states confined to move only on the surface on the Bloch sphere.

In fact, we expect the ensemble ratio of stochastically excited trajectories to increase with increasing η . As mentioned in the main text, trajectories experience $dz < 0$ when the Wiener increment obtained from the measurement record satisfies $dW_t < -\sqrt{\gamma}dt/\sqrt{\eta}x$. Recall that dW_t is a zero-mean random variable distributed with variance dt , and consider the back-action experienced by trajectories initialized with $x = 1$. Naively, the probability of stochastic excitation is then given by the integral,

$$\int_{-\infty}^{-\sqrt{\gamma/\eta}dt} dW_t (2\pi dt)^{-1/2} e^{-dW_t^2/2dt}.$$

As η increases, so does the value of this integral. For $\eta = 1$ and a time step $dt = 20$ ns, the probability for



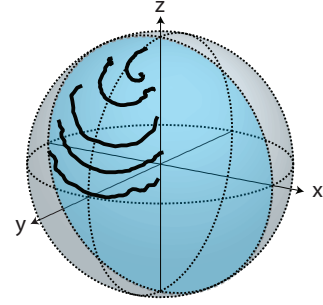
Extended Data Figure 3: **Tomography calibrations.** The ensemble decay as determined by projective measurements for initial states $-z$ (a), and $+x$ (b). c, Tomographic validation for the ensemble of trajectories shows the average tomography values (x, z) versus the values obtained from individual trajectories.

spontaneous emission for our system reaches a maximum value of approximately 41.5%. For our measured quantum efficiency of $\eta = 0.30$, we expect approximately 35% of trajectories to excite in the first time step.

To explore the kinetic dynamics of the individual trajectories decaying from the excited state, we calculate the ensemble averages of the velocity and acceleration of the state at each point in the Bloch sphere. These velocity maps are displayed in Extended Data Fig. 2. We note that in the limit of unity quantum efficiency, the trajectories would remain on the surface of the Bloch sphere and be confined to decay along the meridian crossing $\pm x$. The decay dynamics indicated by these maps mirror the motion of the individual trajectories; for $x > 0$, at first the trajectories have positive \dot{x} and negative \ddot{x} (where the dot denotes differentiation with respect to time), yet when $z > 0$ the sign of \dot{x} reverses. This demonstrates how the deterministic arc expands and contracts as it traverses across the Bloch sphere. Furthermore, the contrasting signs between \dot{x} and \ddot{x} , for trajectories closer the edge of the sphere with $z < 0$, provide a justification for why some trajectories may be pinned to the edges of the deterministic arc. Meanwhile, trajectories in the middle of the sphere experience no preferential acceleration to one direction or another, and can oscillate around $x = 0$ as they diffuse toward the ground state.

Tomography and readout calibration

All tomography results are corrected for imperfect state preparation and readout fidelities. We perform state readout by first applying a resonant pulse at 6.73 GHz to transfer the excited state population to a higher excited state, and then proceeding to drive the bare cavity resonance 6.95 GHz at high power to conduct the Jaynes-Cummings high power readout technique³¹. Tomography along the y and x axes is achieved by first applying a 40 ns $\pi/2$ rotation about the \hat{x} or \hat{y} axes. The combined state preparation and readout fidelity (80%)



Extended Data Figure 4: **Spontaneous decay from the state $+y$.** The emitter's state at different times conditioned on the integrated homodyne measurement signal. The decay times are 80, 160, 320, 640, 960 ns, and the data correspond to what is depicted in Fig. 2f. The $x-z$ plane plotted in Fig. 2f is highlighted in blue.

was determined from the contrast of resonant Rabi oscillations. Each experimental sequence includes separate calibration measurements used to determine the readout level of the ground state and the prepared excited state. These levels are used to scale the tomography results. Extended Data Figure 3a,b shows the ensemble decay curves for the state preparations $-z$ and $+x$.

The emitter's state, given by Bloch coordinates (x, z) , allows us to make predictions for the average outcome of projective measurements on the emitter's state. To characterize accuracy of the state tracking, we compare the predicted values \tilde{x} , \tilde{z} from these coordinates, to the values obtained with projective measurements. In Fig. 4 we apply this to reconstruct an individual trajectory. To accomplish this, we denote an individual trajectory $(\tilde{x}(t), \tilde{y}(t), \tilde{z}(t))$ (Note that $\tilde{y}(t) = 0$). At each time point, we perform several experiments of total duration t' , followed by one of three tomography and readout sequences. For each of these experiments, we calculate $(x(t'), z(t'))$; if $x(t')$ and $z(t')$ are within ± 0.12 of $\tilde{x}(t')$ and $\tilde{z}(t')$, then the subsequent tomography result is included in the tomographic validation at t' . We follow this process for each t' along the trajectory, resulting in a tomographic reconstruction of the trajectory.

We can further test the predictions given by the individual trajectories for all runs of the experiment at all times. Extended Data Figure 3c displays the average projective measurement outcomes conditioned on the values of $\tilde{x}(t')$ or $\tilde{z}(t')$ compared to the values $\tilde{x}(t')$ or $\tilde{z}(t')$ showing good agreement between the individual trajectories and the projective measurements.

Phase-sensitive back-action

When the emitter is initialized in $+y$ the state dynamics are not confined to the $x-z$ plane. Extended Data Figure 4 displays the state conditioned on the integrated homodyne signal and shows how the y -component does not acquire a correlation with the measurement signal. This may be understood as a result of phase-sensitive amplification. When we perform our homodyne measurement of the real part of σ_- , we de-amplify the quadra-

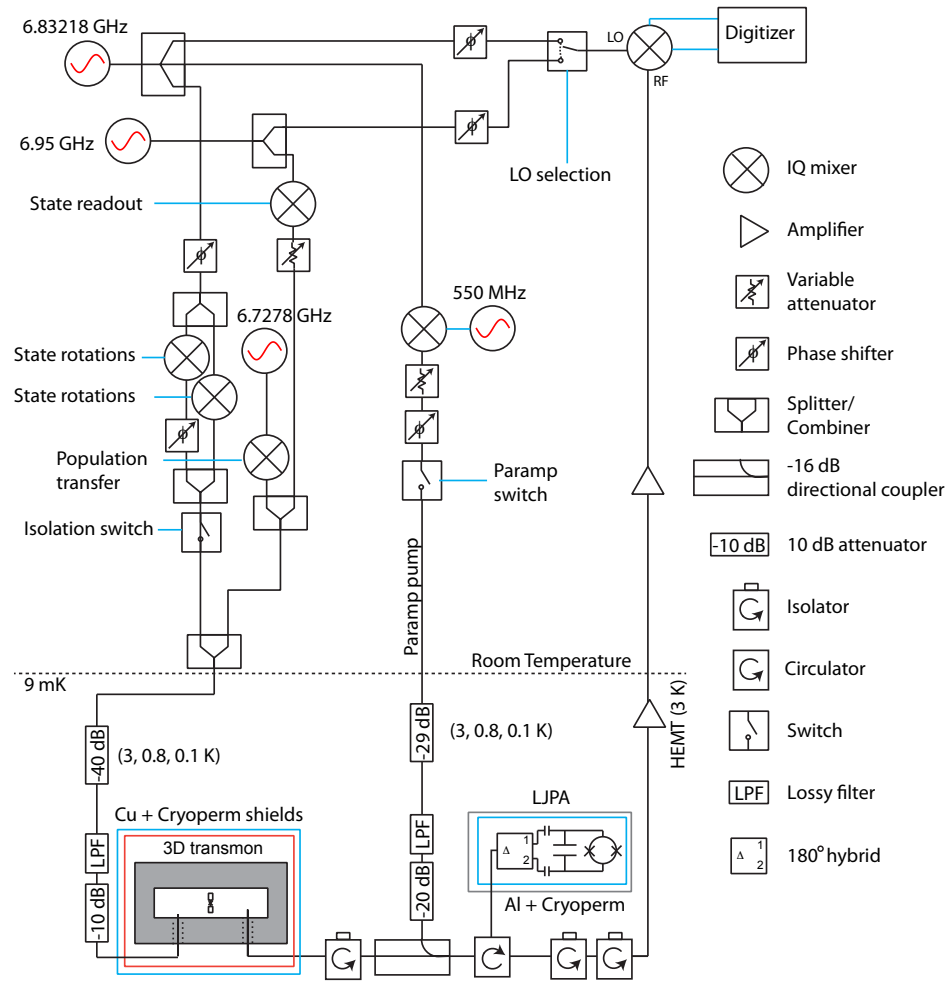
ture containing information on the imaginary part of σ_- , corresponding to σ_y on the Bloch sphere. When this orthogonal signal is de-amplified, we effectively eliminate the information the σ_y quadrature of the emitter's dipole. Therefore we do not perform weak measurements of σ_y , and we do not observe quantum dynamics such as stochastic excitation.

We may also understand this phenomenon by examining the dz and dy segments of the stochastic master equation provided in the main text. The presence of an xy coefficient on the measurement term in Eq. (4), means the stochastic back-action has no effect on the state when it is in an eigenstate of σ_x or σ_y , limiting dynamics to a deterministic reduction in y . Meanwhile, if we examine Eq. (3) after factoring out a common factor of $(1 - z)$ (which serves to push the trajectory toward the ground state) we see the measurement term is pro-

portional only to x . Therefore, for a state prepared with $y = \pm 1$, there will be no initial stochastic excitation, and the state will begin its decay by deterministically approaching the ground state. However, once fluctuations in the measurement signal cause the state to acquire a nonzero x value, the trajectory's dynamics will cease to be trivial.

Experimental setup

Extended Data Figure 5 displays a simplified schematic of the experimental setup. A single generator is used for qubit rotations, the amplifier pump, and demodulation of the amplified signal. The parametric amplifier is pumped by two sidebands that are equally separated from the carrier by 550 MHz, allowing for phase-sensitive amplification without leakage at the emitter's transition frequency. The experimental repetition rate is 8 kHz.



Extended Data Figure 5: **Experimental setup.**